ARTICLE

doi:10.1038/nature11039

Multiple dynamic representations in the motor cortex during sensorimotor learning

D. Huber[1]†*, D. A. Gutnisky[1]*, S. Peron[1], D. H. O'Connor[1], J. S. Wiegert[2], L. Tian[1], T. G. Oertner[2], L. L. Looger[1] & K. Svoboda[1]

The mechanisms linking sensation and action during learning are poorly understood. Layer 2/3 neurons in the motor cortex might participate in sensorimotor integration and learning; they receive input from sensory cortex and excite deep layer neurons, which control movement. Here we imaged activity in the same set of layer 2/3 neurons in the motor cortex over weeks, while mice learned to detect objects with their whiskers and report detection with licking. Spatially intermingled neurons represented sensory (touch) and motor behaviours (whisker movements and licking). With learning, the population-level representation of task-related licking strengthened. In trained mice, population-level representations were redundant and stable, despite dynamism of single-neuron representations. The activity of a subpopulation of neurons was consistent with touch driving licking behaviour. Our results suggest that ensembles of motor cortex neurons couple sensory input to multiple, related motor programs during learning.

Animals move their sensors to collect information, and these movements are guided by sensory input. When action sequences are required to achieve success in novel tasks, interactions between movement and sensation underlie motor control[1] and complex learned behaviours[2]. The motor cortex has important roles in learning motor skills[3–6], but its function in learning sensorimotor associations is unknown.

The neural circuits underlying sensorimotor integration are beginning to be mapped. Different motor cortex layers harbour excitatory neurons with distinct inputs and projections[7–10]. Outputs to motor centres in the brain stem and spinal cord arise from pyramidal-tract-type neurons in layer 5B (L5B). Within motor cortex, excitation descends from L2/3 to L5 (refs 9–11). Input from somatosensory cortex impinges preferentially onto L2/3 neurons[8,12]. L2/3 neurons therefore directly link somatosensation and control of movements.

L2/3 neurons also participate in learning-related plasticity. Synapses from the somatosensory cortex to L2/3 neurons are critical for learning new motor skills[13] and support long-term potentiation[14]. Learning causes plasticity in networks of L2/3 cells[5,15]. L2/3 neurons are thus poised to organize learned movements and the underlying sensorimotor associations.

To define their roles in learning we imaged large L2/3 neuron populations in the vibrissal motor cortex (vM1) while mice learned a sensorimotor task involving whisking and object detection, followed by licking for a water reward. The vM1 is a subdivision of the primary motor cortex in which low-intensity stimulation evokes whisker movements[8,16–18]. Pyramidal-tract-type neurons in vM1 project to the brainstem to control whisking[19,20] and rhythmic licking[5,21]. Activity in the vibrissal somatosensory cortex (vS1; also known as the barrel cortex), activated by touch, propagates to vM1 (refs 18, 22, 23) to excite L2/3 neurons[8,12]. Thus, L2/3 cells in vM1 may directly mediate the stimulus–response (touch–lick) association learned in the object-detection task.

Tracking neuronal populations during learning is challenging because only a small fraction of neurons can be recorded stably over days using electrophysiological methods[24]. Instead, we imaged activity in large populations of neurons[5,25,26] over weeks while monitoring multiple sensory and motor variables[27,28], enabling us to relate population activity to behaviour during learning. Activity in L2/3 cells correlated with licking, whisker movements (whisking) and touch-related forces. Representations of individual neurons changed with learning, but in a restricted manner so that licking neurons rarely changed into whisking neurons and vice versa. This indicates that motor cortex neurons default to represent specific behavioural features. As mice became expert at the sensorimotor task, representations at the level of neuronal populations stabilized, despite continuing changes at the level of individual neurons. A subpopulation of neurons seemed to trigger licking in response to whisker touch, suggesting that L2/3 cells in the motor cortex learn to link task-related sensory inputs and actions.

Learning under the microscope

We trained head-fixed mice in a vibrissa-based object-detection task[27] while imaging populations of neurons (Fig. 1a)[28]. Following a sound, a pole was moved to one of several target positions within reach of the whiskers (the 'go' stimulus) or to an out-of-reach position (the 'no-go' stimulus) (Fig. 1b). Target and out-of-reach locations were arranged along the anterior–posterior axis; the out-of reach position was most anterior (Fig. 1a). Mice searched for the pole with one whisker row (the C row) and reported the pole as 'present' by licking, or 'not present' by withholding licking. Licking on go trials (hit) was rewarded with water, whereas licking on no-go trials (false alarm) was punished with a time-out during which the trial was stopped for 2 seconds. Trials without licking (no-go, correct rejection, go, and miss) were not rewarded or punished. All mice showed learning within the first two or three sessions ($d' > 0.8$, one-tailed bootstrap test, $P < 0.001$) (Fig. 1c). Performance reached expert levels after three to six training sessions ($d' > 1.75$, approximately 80% correct trials, $P < 0.001$).

We used videography and automated whisker tracking (Fig. 1a)[27] to determine the whisker movements and somatosensory input. Rhythmic whisking (10–20 Hz) was superposed on slower changes

[1]Janelia Farm Research Campus, Howard Hughes Medical Institute, 19700 Helix Drive, Ashburn, Virginia 20147, USA. [2]Center for Molecular Neurobiology Hamburg, Falkenried 94, 20251 Hamburg, Germany. †Present address: Department of Basic Neurosciences, University of Geneva, CH-1211 Geneva, Switzerland.
*These authors contributed equally to this work.

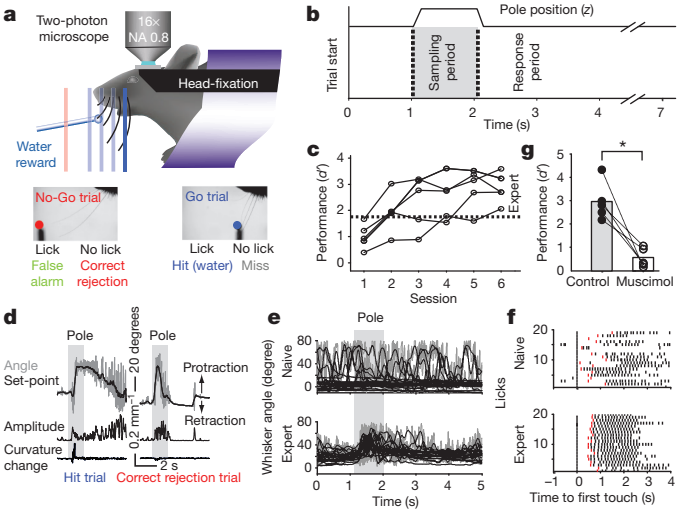

Figure 1 | Learning a whisker-based object-detection task under the microscope. **a**, A head-fixed mouse under a two-photon microscope. Whisker movements were tracked with high-speed videography. For each trial, a metal pole was presented either within reach of the whiskers (in one of several target locations, corresponding to different hues of blue; go trial) or out of reach (red, no-go trial). **b**, Onset of pole movement produced an auditory cue (vertical dotted lines). The pole was within reach in the sampling period. Answer licks were scored in the response period. **c**, Learning curves. The sensitivity index d' measures behavioural performance ($d' = 0$, chance performance; $d' = 1.75$, expert level (above the dashed line) approximately 80% correct trials). **d**, Whisker movement and forces. Top traces, trial showing whisker angle (grey) and set point (black). Middle traces, whisking amplitude (see Methods). Bottom traces, change in whisker curvature, which is proportional to force acting on the follicle. Left, hit trial; right, correct rejection trial. **e**, Learning-related changes in whisking. Whisker angle (measured at the base of the whisker, grey) and set point (low-pass filtered angle, black) for 20 consecutive correct rejection trials in the first (top; $d' = 0.83$, first session) and fifth session (bottom; $d' = 3.52$). **f**, Learning-related changes in licking. Licks (ticks; answer licks in red) aligned to first touch, for 20 consecutive hit trials of a naive mouse (top; $d' = 0.83$) and of the same animal but in the fourth session (bottom; $d' = 3.59$). **g**, Behavioural performance drops after inactivation of vM1 ($n = 5$ mice; control, solid circles; muscimol, open circles; asterisks, $P < 0.001$).

in the average whisker position, the set point (Fig. 1d, e). Whisking was thus split into set point (<6 Hz) and amplitude (6–60 Hz; Methods)[29] (Fig. 1d). As a measure of sensory input, we extracted touch-induced changes in whisker curvature, which are proportional to the pressure activating mechanoreceptors in the follicle[30,31].

Improved performance in the object-detection task correlated with changes in motor behaviour. Naive mice whisked occasionally, in a manner that was unrelated to the trial structure (Fig. 1e), probably reflecting their uncertainty about the stimulus–response relationship. In contrast, expert mice protracted their whiskers through a large angle to search for the pole soon after it became available (within approximately 350 ms) (auditory cue, Fig. 1d, e)[27]. The repeatability of whisking across trials (Pearson's correlation coefficient; $\rho = 0.57$, $P < 0.001$) (Supplementary Fig. 1a and Methods) and the amplitude of whisker protraction during the sampling period increased with performance ($\rho = 0.54$, $P < 0.001$) (Supplementary Fig. 1b). Licking consisted of rhythmic bouts of 7.2 ± 0.45 Hz[5,21] (Fig. 1f). The timing of lick bouts with respect to touch became stereotyped with learning. Naive mice licked with variable latencies (on hit trials), and licking sometimes even preceded touch, indicating that the mice were guessing. Expert mice licked shortly after first touch, and the temporal jitter of the first lick in a bout decreased with performance ($\rho = -0.50$, $P < 0.001$) (Supplementary Fig. 1c).

Thus, object detection relies on a sequence of actions, linked by sensory cues. An auditory cue triggers whisking during the sampling period. Contact between whisker and object causes licking for a water reward during a response period. Silencing vM1 indicates that this task requires the motor cortex. With vM1 silenced, task-dependent whisking persisted, but was reduced in amplitude and repeatability (Supplementary Figs 1 and 2), and task performance dropped (permutation test; $P < 0.001$) (Fig. 1g and Supplementary Fig. 1e). Similar experiments revealed that vS1 is also crucial for the object-detection task (Supplementary Fig. 1f)[27,32]. These observations suggest that vM1 and vS1 have critical roles in linking sensation and movement.

Chronic imaging of population activity

L2/3 cells in vM1 may directly mediate the learned association between whisking, touch and licking. We therefore imaged the activity of L2/3 neurons during learning (Fig. 2). To target vM1 for imaging we injected adeno-associated virus (AAV) expressing tdTomato[33]

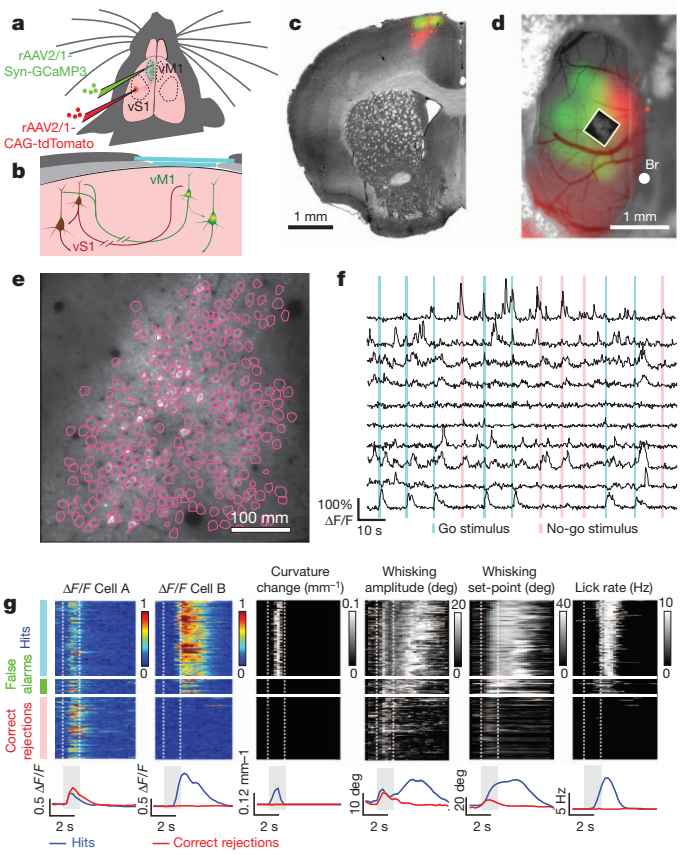

Figure 2 | Imaging population activity across trials. **a**, Injection sites for GCaMP3 virus in vM1 and tdTomato virus in vS1. rAAV2/1-CAG-tdTomato, recombinant AAV serotype 2/1 (rAAV2/1) virus expressing tdTomato under the *CAG* promoter; rAAV2/1-Syn-GCaMP3, rAAV2/1 virus expressing GCaMP3 under the human synapsin 1 promoter. **b**, L2/3 neurons in vM1 receive strong input from vS1 and excite deep layer neurons in vM1. Light blue, glass imaging window; light grey, bone; dark grey, dental cement. **c**, **d**, GCaMP3 (green) and tdTomato (red) fluorescence image overlaid on a bright-field image (grey), in coronal section (**c**) and through the imaging window (**d**). Box, field of view in **e**. Br, Bregma. **e**, L2/3 neurons expressing GCaMP3 (depth, 210 μm). Individual regions (individual neurons) are outlined in pink. **f**, Example fluorescence traces (fractional change in fluorescence, $\Delta F/F$; ten neurons in twelve trials). Vertical bars, sampling period (blue, go trials; red, no-go trials). **g**, Example neurons (cells A and B) across one session (329 trials; expert mouse, $d' = 3.13$) and simultaneously recorded behaviours. Consecutive hit, false alarm and correct rejection trials are arrayed from top to bottom (misses were rare in this session). Fluorescence intensity was normalized. Curvature changes due to touch only occur during the sampling period in hit trials, because otherwise the pole was out of reach. Whisking occurred in all trials. Licking occurred in hit and false alarm trials. Lower panel, session averages for correct trial types (blue, hits; red, correct rejections). Deg, degrees.

into the C2 column of vS1 and visualized red axonal fluorescence in vM1 (Fig. 2a–d; see Methods). We infected vM1 with the genetically encoded calcium indicator GCaMP3 (ref. 34). Long-term expression of GCaMP3 did not cause detectable damage *in vivo*, and it did not inhibit long-term potentiation in brain slices (Supplementary Figs 3 and 4).

We imaged GCaMP3-expressing neurons through an imaging window[35] in fields of view overlapping with the red axons (Fig. 2c–e). Images (approximately 250 neurons; Supplementary Table 1) were acquired continuously (4 Hz) over sessions lasting 1 h (280 trials; range of 141–424 trials). Regions of interest were drawn around individual cells to extract fluorescence dynamics caused by neural activity (Fig. 2e and Supplementary Fig. 5). A deconvolution algorithm was used to detect fluorescence events[36] corresponding to small bursts of action potentials (>2 action potentials)[34] (Supplementary Fig. 5 and Methods). Events were detected in 10.6% of neurons per session (Methods and Supplementary Table 1) (Fig. 2f). Of all neurons, 43% showed activity in at least one session. All subsequent analyses were based on these 'events' (286 unique neurons; >10 events per session; 5 animals; 6 sessions per animal). Time series of events were aligned with recordings of behaviour, such as whisking, licking and touch, and grouped by trial type (hit, correct rejection, miss and false alarm) (Fig. 2g).

Intermingled representations in the motor cortex

L2/3 cells in vM1 receive strong input from vS1. To investigate which behaviours are represented by L2/3 cells during active somatosensation, we quantified how well specific behavioural variables could be decoded from neural activity[37]. We used random forests[38], a generalized form of regression (Methods), to decode behaviour based on all neurons (Fig. 3). Each behavioural session was treated separately. The behavioural features measured touch (whisker curvature changes; Fig. 1d) and movements (whisking set-point, whisking amplitude and licking; Methods and Fig. 1d, f). The algorithm used the activity of populations of neurons to fit individual behavioural features (the 'model'), taking into account dynamics within and across trials (Fig. 3). The explained variance (R_i^2, for the ith behavioural feature) was used to measure the quality of decoding.

Population activity typically accounted for the recorded behavioural features with high fidelity. The model captured the timing of contact between whisker and object (Fig. 3a) (range of R^2 values was 0.03–0.55 for individual mice and sessions). Coding of touch in the motor cortex[18,22] is consistent with direct input from vS1 to the imaged neurons[8]. The model also predicted motor behaviours (Fig. 3b–e) (whisking amplitude, range of R^2, 0.22–0.60; whisker set-point, range of R^2, 0.22–0.66; lick rate, range of R^2, 0.13–0.75). Accurate decoding of whisking amplitude, whisking set-point and lick rate suggests that vM1 controls these slowly varying motor parameters, as expected from previous motor cortex mapping[5,8,16,18,29,39] and neurophysiological experiments[5,29,39]. The low sampling rate of imaging may have missed rapid modulation in neural activity[29].

We also quantified decoding accurancy as a function of the number of neurons (Supplementary Fig. 6). Each behavioural feature required only a very low number of neurons (1.5–5.5) to reach saturating decoding performance. This suggests that the representations underlying object localization are redundant.

We next asked how individual neurons contribute to the population representation. Correlations between activity of individual neurons and specific behaviours were apparent in the raw traces. For example, some neurons were active at the same time as whisking during the sampling period, independent of trial type (cell A, Fig. 2g), whereas other neurons were active only during licking (cell B, Fig. 2g) or during other phases of the task (Supplementary Figs 7–13).

To quantify neuronal representations we used random forests again, but this time behavioural features were fit using single neurons. The explained variance (R_i^2, for the ith behavioural feature) was used to measure the quality of decoding by single neurons. Almost one-half of the active neurons (42%) decoded one or more of the measured behavioural features (mean R_i^2 for the feature that was decoded best, 0.22) (Supplementary Fig. 7), with varying degrees of reliability (Supplementary Fig. 14a–k). Shuffling the trial labels caused the quality of the fit to decrease ($R_i^2 > R_{i,\ \mathrm{shuffled}}^2$, $P < 0.05$ for 351 out of 358 neurons; 1,000 shuffles; average z score, 31; Supplementary Fig. 14l, m), indicating that the random forest algorithm captured the covariance of activity and behaviour within trials as well as across trials.

We classified neurons into categories (touch, whisking and licking), mainly based on the largest correlation coefficient (maximum R_i^2) (Supplementary Fig. 7). However, one of the trial types was sometimes more informative than other trial types and caused the largest overall correlation coefficient to be overruled (Methods) (Supplementary Figs 7–13). For example, the relationship between neuronal activity and whisking was only evaluated in trials without touch and licking (correct rejections). In addition, we considered correlations between activity and sensory variables (object location or forces acting on the whisker, Supplementary Figs 10, 13 and 15). For example, in hit trials some licking neurons showed activity levels that varied with object location, a signature of sensory input (Supplementary Figs 8, 11, 13

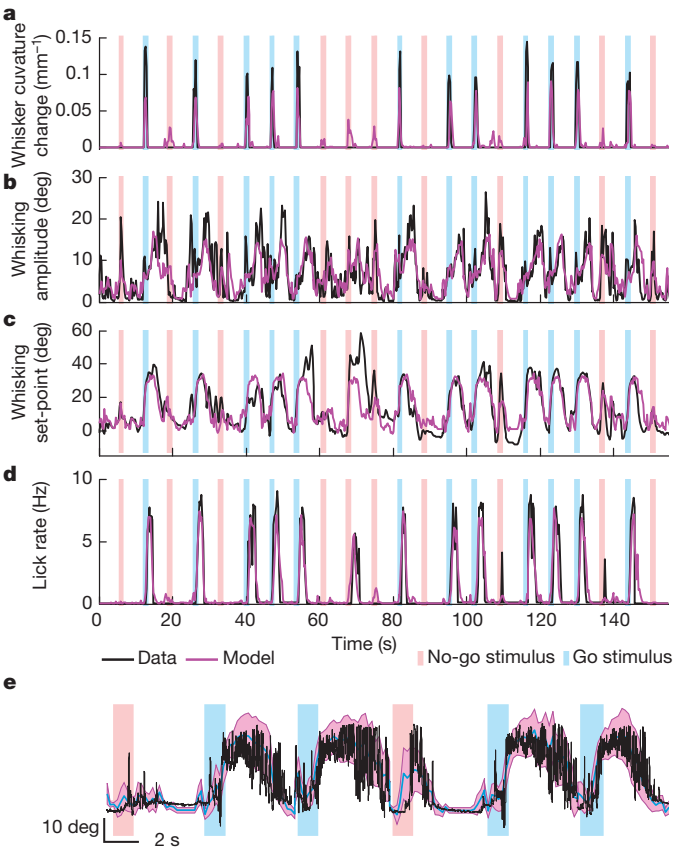

Figure 3 | Population decoding of behavioural features. a–d, Time series of behavioural features (black; down-sampled to the imaging rate, 4 Hz) and a model based on the activity of all active neurons in one session (magenta) (same session as in Fig. 2g). Vertical bars, sampling period (blue, go trials; red, no-go trials). The behavioural features measured are whisker curvature change (**a**), whisking amplitude (**b**), whisking set-point (**c**) and lick rate (**d**). Shuffling trial labels dropped the quality of the fit for all behavioural features. $R_i^2 > R_{\mathrm{i\ shuffled}}^2$, $P < 0.001$ for all sessions and animals except for three sessions in which coding of touch was weak (mean z scores (1,000 shuffles): whisking amplitude, 73; whisking set-point, 28; licking, 23; touch, 10; see Supplementary Fig. 14l, m for an explanation of z scores). **e**, Overlay of whisking at full bandwidth (black) and the model (thick blue trace, whisking set-point; magenta band, whisking set-point ± whisking amplitude). Deg, degrees.

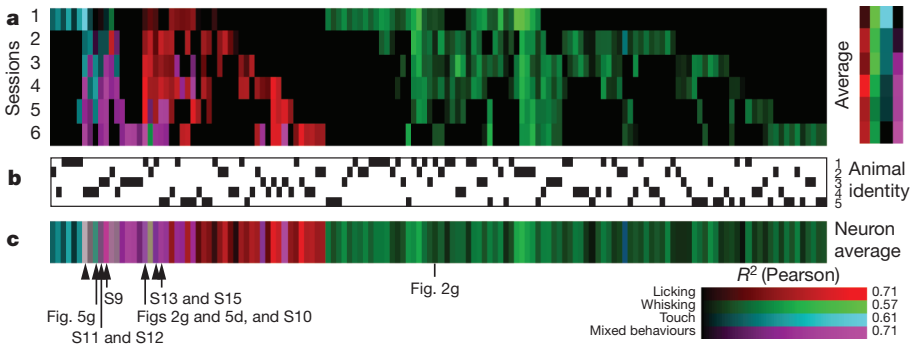

Figure 4 | Single neuron representations across learning. **a**, Dynamics of classified neurons during learning (cyan, touch; magenta, mixed; red, licking; green, whisking). Each column corresponds to one neuron. The intensity of the colour indicates the correlation (R^2) between data and the model (Methods). Session 1, naive mice; session 6, expert mice. **b**, Animal identity. Each row corresponds to one animal. Black ticks indicate the animal corresponding to the classified cell. **c**, Classification of individual neurons averaged across sessions. Arrowheads, neurons with object location-dependent activity. Tagged neurons, data shown in other figures. S, Supplementary Information figure.

and 15). Such neurons, which correlated with multiple behavioural features, were classified as 'mixed' neurons (see Supplementary Fig. 7 and Methods for a full explanation of the classification rules).

The other active neurons remained unclassified on the basis of the measured behavioural features (mean R_i^2 for best feature, 0.03). However, these neurons still showed interpretable task-related activity (Supplementary Fig. 7). Some neurons became active during errors and others while withholding licking[5]. Together, the unclassified neurons might have roles in cognitive processes; alternatively, they might relate to motor or sensory variables that were not tracked in our study. Overall, only a small fraction of active vM1 neurons expressed any one representation (3% touch, 26% whisking, 9% licking and 4% mixed), suggesting sparse coding of multiple behavioural features in vM1.

Dynamics of representations with learning

We next investigated how individual neurons change with learning. We used the classification of individual neurons to track changes in representations over learning (6 sessions, corresponding to 6–14 days; Methods and Supplementary Fig. 5). Single neurons were dynamic (Fig. 4 and Supplementary Fig. 16): cells that decoded a given feature during one session often did not contribute during other sessions, and vice versa. However, when a neuron was classified in different sessions it decoded similar behavioural features (Supplementary Table 2) so that most neurons were classified as part of no more than one representation throughout learning (Fig. 4a, c). In particular, whisking neurons rarely became licking neurons and vice versa.

All response categories were detected in all animals (Fig. 4a, b and Supplementary Fig. 7) and the representations were spatially intermingled (Supplementary Fig. 16); nearby neurons were equally likely to be part of any of the representations (spatial clustering index (SCI), ~1.0). These data suggest that motor cortex contains intermingled representations of different movements, and that individual neurons are primed to participate in controlling specific movements.

Learning also altered the timing of neuronal activity. In naive mice, activity was distributed uniformly across the trial (Fig. 5a). With learning, activity of the classified neurons (but not the unclassified neurons) shifted towards the sampling period (Fig. 5b, c and Supplementary Fig. 17). The fraction of neurons that were most active in the sampling period increased by a factor of three, with little change in overall activity levels (Supplementary Fig. 17). These shifts in activity were explained in part by changes in whisking, which became more concentrated in the sampling period with learning (Fig. 1e), and a shorter touch–lick latency (Supplementary Fig. 1). With learning, licking neurons became active earlier within the trial and also began to fire earlier with respect to licking. In naive mice, activity in licking

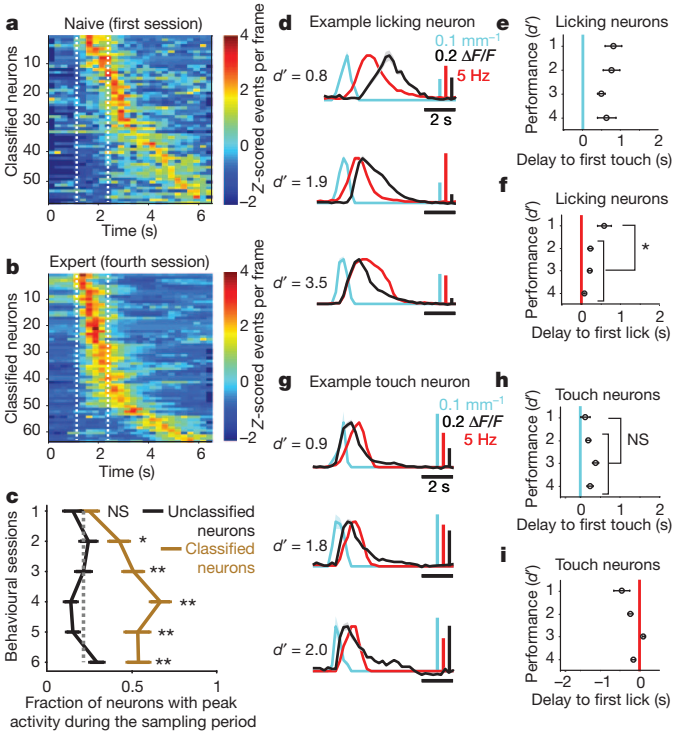

Figure 5 | Plasticity in task-related neuronal dynamics. **a**, **b**, Trial averages of all classified neurons, ordered by the timing of their peak activity. **a**, Naive mice (first session). **b**, Expert mice (fourth session). **c**, Fraction of neurons with peak activity during the sampling period of classified (brown) and unclassified neurons (black) as a function of learning (mean ± s.e.m., $n = 5$ mice). The grey dotted line indicates the expected fraction of neurons if the timing of peak activity was uniformly distributed across the trial (*$P < 0.05$; **$P < 0.005$; χ^2 test for each session). **d**–**i**, Temporal parameters of licking and touch neurons as a function of task performance. Performance (d') was binned as follows: 1, <1.75; 2, 1.75–2.5; 3, 2.5–3.5; 4, >3.5. **d**, Peristimulus time histograms (PSTHs) of touch (cyan, change in whisker curvature), lick rate (red) and fluorescent traces of a representative licking neuron (black) in a naive mouse (top trace), a mouse during learning (middle trace) and an expert mouse (bottom trace). **e**, Delay from first contact to activity onset in licking neurons (12 neurons, decoding licking for at least 4 days; mean ± s.e.m.). **f**, Delay from first lick to activity onset in licking neurons. The delay shortened after learning (*$P <$ 0.005, Wilcoxon rank sum test). **g**, PSTHs of touch (cyan, change in whisker curvature), lick rate (red) and fluorescent traces of a representative touch neuron (black) in a naive mouse (top trace), a mouse during learning (middle trace) and an expert mouse (bottom trace). **h**, Delay from first contact to activity onset in touch neurons (12 neurons from 4 animals). **i**, Delay from first lick to activity onset in touch neurons.

neurons trailed licking (Fig. 5d–f); in expert mice, activity anticipated licking (when the slow kinetics of GCaMP3 fluorescence were taken into account[34]). Licking neurons always lagged the first touch (Fig. 5e), as did touch neurons (Fig. 5g, h). These learning-related changes in temporal relationships between activity and motor behaviour suggest roles of these neurons in controlling movement. Furthermore, nearby neurons can participate in highly specific forms of circuit plasticity during learning.

We next analysed the dynamics of population-level representations during learning (Fig. 6a–c). We decoded the behavioural features over all experimental sessions and evaluated the quality of the fit as a function of behavioural performance (Fig. 6a). Overall, the representation of licking strengthened, even though the number of licks per trial remained stable during learning (Supplementary Fig. 17e). In contrast, the representation of whisking remained stable, even though whisking during the sampling period became more vigorous and purposeful (Fig. 1e and Supplementary Fig. 1).

We assessed the stability of population representations by using the model derived in one session to predict the behavioural features of another session (Fig. 6b). For the first two or three sessions the models derived on one day failed to predict movements on subsequent days, implying labile population representations. However, as the behaviour reached a plateau level the representations stabilized, particularly for whisking and licking. More than 44% of the variance in the change in behavioural performance between any two sessions could be explained on the basis of changes in the representations of the different behavioural features (multiple linear regression; $P < 10^{-17}$; $F_{4,145} = 29$). Changes in the representation of licking were more predictive of the behavioural performance changes than whisking or touch (Fig. 6c). The dynamics of the different representations suggest that vM1 innately controls whisking but participates in the control of licking only in the context of specific sensorimotor contingencies, such as licking triggered by touch.

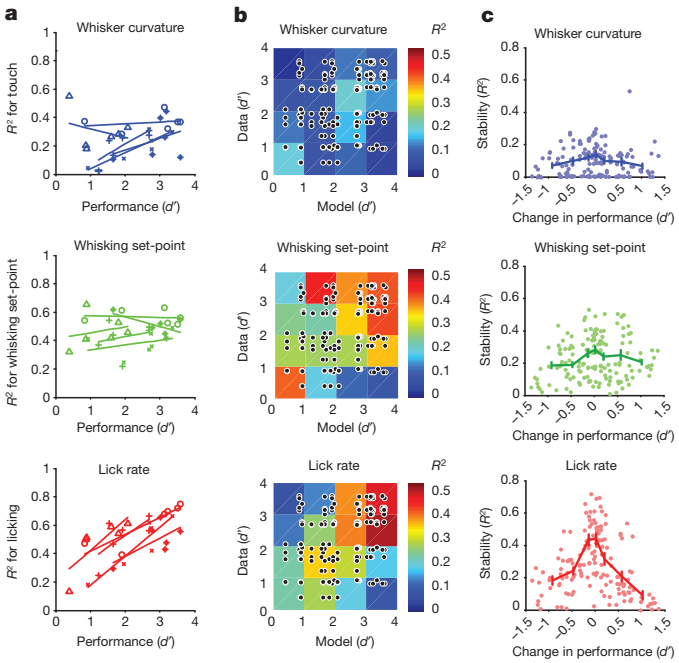

Figure 6 | Stability in population decoding. a, Decoding of behavioural features as a function of behavioural performance. Individual animals correspond to different symbols; lines are linear fits. Top, whisker curvature; middle, whisking set-point; bottom, lick rate. Whisking amplitude was similar to whisking set-point and is not shown. **b**, Matrix of correlation coefficients for all mice, binned and averaged by behavioural performance (d'). Each point corresponds to a model derived at one value of d' applied to a session with another value of d' . The points corresponding to models and data from the same session (diagonal) were excluded. **c**, Stability of population decoding of behavioural features (change in R^2) as a function of change in behavioural performance. Points are derived as in **b**. Changes in the representation of licking were more predictive with respect to changes in behavioural performance than whisking or touch: licking, $R^2 = 0.39$, $F_{1,148} = 94$, $P < 10^{-17}$; whisking set-point, $R^2 = 0.21$; $F_{1,148} = 40$, $P < 10^{-17}$; touch $R^2 = 0.07$; $F_{1,148} = 11$, $P < 0.001$; licking versus set point, $P < 0.001$, Ansari–Bradley test.

Discussion

The precise roles of motor cortex in shaping movement and motor learning have been debated for more than a century (reviewed in refs 1, 40). Classic recordings from identified pyramidal-tract-type neurons, which carry cortical output to motor centres, revealed activity related to muscle forces and movements[41]. However, pyramidal-tract-type neurons constitute only a tiny fraction of motor cortex neurons[7]. Simultaneous recordings from diverse neuron types indicate that neuronal ensembles define trajectories of multi-joint movements[26,42]. Conversely, stimulating groups of motor cortex neurons on behavioural timescales evokes complex, ethologically relevant movements[43]. vM1 projects to brainstem nuclei that control facial motor programs such as whisking[19,20] and licking[5]. Our imaging experiments in vM1 show spatially intermingled representations of various facial movements (Supplementary Fig. 16), all of which are related to performing the object-detection task (Figs 1 and 3). Together, these observations suggest that small regions of motor cortex help to orchestrate goal-directed movements involving multiple body parts.

Motor cortex activity changes with learning[3–5]. Goal-directed movements might therefore be established or fine-tuned in the motor cortex. Consistent with this view, representations in L2/3 of motor cortex changed during learning of the object detection task. However, individual L2/3 neurons seem to be pre-wired to represent particular motor variables: whisking neurons rarely became licking neurons and vice versa (Fig. 4). In expert animals, population-level representations were stable (Fig. 6), even with unstable representations of single neurons (Fig. 4 and Supplementary Fig. 16). Theoretical work has shown that drifting representations at the level of individual neurons may be crucial for motor learning[4].

The representation of whisking was strong in L2/3 neurons of naive animals and remained strong throughout learning (Fig. 6). In contrast, the representation of licking increased with improvements in behavioural performance. Control of voluntary whisking might therefore be innate to vM1, whereas vM1 assumes control of licking as the animal learns to initiate licking in response to a specific sensory stimulus (for example, touch (Fig. 1) or olfaction[5]). Enabling flexible associations between sensation and action could be a core function of the superficial layers of the motor cortex.

To investigate the cellular mechanisms driving changes in vM1 activity, we used an object-location task. Learning this task requires chaining a set of sensory-modulated actions into a specific order. Behaviourally, we observed that stereotypic whisking and latency between touch and licking were highly correlated with task proficiency (Fig. 1). Early during learning, activity of L2/3 neurons was distributed uniformly across time, and this might provide a basis from which[2,44] appropriate sequences of movements can be selected, depending on task demands (Fig. 5 and Supplementary Fig. 17). After learning, neurons fired mostly during the sampling period, coincident with whisking, touch and onset of licking. This change of timing suggests a role for a dopaminergic reward prediction error signal[45], probably arising in the ventral tegmental area[6], which could implement temporal credit assignment in synaptic plasticity[2].

METHODS SUMMARY

We used adult male PV-IRES-cre mice (over 2 months old) (B6;129P2-Pvalbtm1(cre)Arbr/J, The Jackson Laboratory). Details of surgery, imaging and data analysis are provided in Methods.

Full Methods and any associated references are available in the online version of the paper at www.nature.com/nature.

Received 20 August 2011; accepted 12 March 2012.

1. Scott, S. H. Inconvenient truths about neural processing in primary motor cortex. *J. Physiol. (Lond.)* **586,** 1217–1224 (2008).
2. Wolpert, D. M., Diedrichsen, J. & Flanagan, J. R. Principles of sensorimotor learning. *Nature Rev. Neurosci.* **12,** 739–751 (2011).
3. Wise, S. P., Moody, S. L., Blomstrom, K. J. & Mitz, A. R. Changes in motor cortical activity during visuomotor adaptation. *Exp. Brain Res.* **121,** 285–299 (1998).
4. Rokni, U., Richardson, A. G., Bizzi, E. & Seung, H. S. Motor learning with unstable neural representations. *Neuron* **54,** 653–666 (2007).
5. Komiyama, T. *et al.* Learning-related fine-scale specificity imaged in motor cortex circuits of behaving mice. *Nature* **464,** 1182–1186 (2010).
6. Hosp, J. A., Pekanovic, A., Rioult-Pedotti, M. S. & Luft, A. R. Dopaminergic projections from midbrain to primary motor cortex mediate motor skill learning. *J. Neurosci.* **31,** 2481–2487 (2011).
7. Keller, A. Intrinsic synaptic organization of the motor cortex. *Cereb. Cortex* **3,** 430–441 (1993).
8. Mao, T. *et al.* Long-range neuronal circuits underlying the interaction between sensory and motor cortex. *Neuron* **72,** 111–123 (2011).
9. Hooks, B. M. *et al.* Laminar analysis of excitatory local circuits in vibrissal motor and sensory cortical areas. *PLoS Biol.* **9,** e1000572 (2011).
10. Anderson, C. T., Sheets, P. L., Kiritani, T. & Shepherd, G. M. Sublayer-specific microcircuits of corticospinal and corticostriatal neurons in motor cortex. *Nature Neurosci.* **13,** 739–744 (2010).
11. Kaneko, T., Cho, R., Li, Y., Nomura, S. & Mizuno, N. Predominant information transfer from layer III pyramidal neurons to corticospinal neurons. *J. Comp. Neurol.* **423,** 52–65 (2000).
12. Kaneko, T., Caria, M. A. & Asanuma, H. Information processing within the motor cortex. II. Intracortical connections between neurons receiving somatosensory cortical input and motor output neurons of the cortex. *J. Comp. Neurol.* **345,** 172–184 (1994).
13. Pavlides, C., Miyashita, E. & Asanuma, H. Projection from the sensory to the motor cortex is important in learning motor skills in the monkey. *J. Neurophysiol.* **70,** 733–741 (1993).
14. Iriki, A., Pavlides, C., Keller, A. & Asanuma, H. Long-term potentiation in the motor cortex. *Science* **245,** 1385–1387 (1989).
15. Rioult-Pedotti, M. S., Friedman, D., Hess, G. & Donoghue, J. P. Strengthening of horizontal cortical connections following skill learning. *Nature Neurosci.* **1,** 230–234 (1998).
16. Li, C. X. & Waters, R. S. Organization of the mouse motor cortex studied by retrograde tracing and intracortical microstimulation (ICMS) mapping. *Can. J. Neurol. Sci.* **18,** 28–38 (1991).
17. Brecht, M. *et al.* Organization of rat vibrissa motor cortex and adjacent areas according to cytoarchitectonics, microstimulation, and intracellular stimulation of identified cells. *J. Comp. Neurol.* **479,** 360–373 (2004).
18. Ferezou, I. *et al.* Spatiotemporal dynamics of cortical sensorimotor integration in behaving mice. *Neuron* **56,** 907–923 (2007).
19. Hattox, A. M., Priest, C. A. & Keller, A. Functional circuitry involved in the regulation of whisker movements. *J. Comp. Neurol.* **442,** 266–276 (2002).
20. Grinevich, V., Brecht, M. & Osten, P. Monosynaptic pathway from rat vibrissa motor cortex to facial motor neurons revealed by lentivirus-based axonal tracing. *J. Neurosci.* **25,** 8250–8258 (2005).
21. Travers, J. B., Dinardo, L. A. & Karimnamazi, H. Motor and premotor mechanisms of licking. *Neurosci. Biobehav. Rev.* **21,** 631–647 (1997).
22. Kleinfeld, D., Sachdev, R. N., Merchant, L. M., Jarvis, M. R. & Ebner, F. F. Adaptive filtering of vibrissa input in motor cortex of rat. *Neuron* **34,** 1021–1034 (2002).
23. Sato, T. R. & Svoboda, K. The functional properties of barrel cortex neurons projecting to the primary motor cortex. *J. Neurosci.* **30,** 4256–4260 (2010).
24. Ganguly, K. & Carmena, J. M. Emergence of a stable cortical map for neuroprosthetic control. *PLoS Biol.* **7,** e1000153 (2009).
25. Stosiek, C., Garaschuk, O., Holthoff, K. & Konnerth, A. *In vivo* two-photon calcium imaging of neuronal networks. *Proc. Natl Acad. Sci. USA* **100,** 7319–7324 (2003).
26. Dombeck, D. A., Graziano, M. S. & Tank, D. W. Functional clustering of neurons in motor cortex determined by cellular resolution imaging in awake behaving mice. *J. Neurosci.* **29,** 13751–13760 (2009).
27. O'Connor, D. H. *et al.* Vibrissa-based object localization in head-fixed mice. *J. Neurosci.* **30,** 1947–1967 (2010).
28. O'Connor, D. H., Peron, S. P., Huber, D. & Svoboda, K. Neural activity in barrel cortex underlying vibrissa-based object localization in mice. *Neuron* **67,** 1048–1061 (2010).
29. Hill, D. N., Curtis, J. C., Moore, J. D. & Kleinfeld, D. Primary motor cortex reports efferent control of vibrissa motion on multiple timescales. *Neuron* **72,** 344–356 (2011).
30. Birdwell, J. A. *et al.* Biomechanical models for radial distance determination by the rat vibrissal system. *J. Neurophysiol.* **98,** 2439–2455 (2007).
31. Knutsen, P. M. & Ahissar, E. Orthogonal coding of object location. *Trends Neurosci.* **32,** 101–109 (2009).
32. Hutson, K. A. & Masterton, R. B. The sensory contribution of a single vibrissa's cortical barrel. *J. Neurophysiol.* **56,** 1196–1223 (1986).
33. Shaner, N. C. *et al.* Improved monomeric red, orange and yellow fluorescent proteins derived from Discosoma sp. red fluorescent protein. *Nature Biotechnol.* **22,** 1567–1572 (2004).
34. Tian, L. *et al.* Imaging neural activity in worms, flies and mice with improved GCaMP calcium indicators. *Nature Methods* **6,** 875–881 (2009).
35. Trachtenberg, J. T. *et al.* Long-term *in vivo* imaging of experience-dependent synaptic plasticity in adult cortex. *Nature* **420,** 788–794 (2002).
36. Vogelstein, J. T. *et al.* Fast nonnegative deconvolution for spike train inference from population calcium imaging. *J. Neurophysiol.* **104,** 3691–3704 (2010).
37. Graf, A. B., Kohn, A., Jazayeri, M. & Movshon, J. A. Decoding the activity of neuronal populations in macaque primary visual cortex. *Nature Neurosci.* **14,** 239–245 (2011).
38. Hastie, T., Tibshirani, R. & Friedman, J. *The Elements of Statistical Learning* 2nd edn (Springer, 2009).
39. Carvell, G. E., Miller, S. A. & Simons, D. J. The relationship of vibrissal motor cortex unit activity to whisking in the awake rat. *Somatosens. Mot. Res.* **13,** 115–127 (1996).
40. Graziano, M. S. A. *The Intelligent Movement Machine* 1st edn (Oxford, 2009).
41. Evarts, E. V. Relation of pyramidal tract activity to force exerted during voluntary movement. *J. Neurophysiol.* **31,** 14–27 (1968).
42. Afshar, A. *et al.* Single-trial neural correlates of arm movement preparation. *Neuron* **71,** 555–564 (2011).
43. Graziano, M. S. & Aflalo, T. N. Mapping behavioral repertoire onto the cortex. *Neuron* **56,** 239–251 (2007).
44. Salinas, E. Rank-order-selective neurons form a temporal basis set for the generation of motor sequences. *J. Neurosci.* **29,** 4369–4380 (2009).
45. Schultz, W., Dayan, P. & Montague, P. R. A neural substrate of prediction and reward. *Science* **275,** 1593–1599 (1997).

Supplementary Information is linked to the online version of the paper at www.nature.com/nature.

Acknowledgements We thank B. Ölveczky, L. Petreanu, N. Li, A. Hantman and S. Druckmann for critical comments on the manuscript; N. Clack, V. Iyer and J. Vogelstein for help with software; D. Flickinger for help with microscope design; J. Kim for tdTomato adeno-associated virus; N. Xu for suggestions regarding mouse behaviour; and T.-W. Chen and E. Schreiter for help with calibrating GCaMP3.

Author Contributions D.H. and K.S. conceived the study. D.H. performed all behavioural and *in vivo* imaging experiments. J.S.W. performed the LTP experiments. D.H., D.A.G., S.P. and K.S. performed analysis. D.A.G., S.P. and D.H.O. provided software. L.T., T.G.O. and L.L.L. provided reagents. D.H., D.A.G. and K.S. wrote the paper with comments from all authors.

Author Information Reprints and permissions information is available at www.nature.com/reprints. The authors declare no competing financial interests. Readers are welcome to comment on the online version of this article at www.nature.com/nature. Correspondence and requests for materials should be addressed to K.S. (svobodak@janelia.hhmi.org).

METHODS

Chronic window preparation. All procedures were approved by the Janelia Farm Research Campus Institutional Animal Care and Use Committee. We used adult (older than postnatal day 60) male PV-IRES–Cre (parvalbumin internal ribosomal entry site (IRES) Cre recombinase) mice (B6;129P2-Pvalbtm1(cre)Arbr/J, The Jackson Laboratory). All surgeries were conducted under isoflurane anaesthesia (1.5–2%). Additional drugs reduced potential inflammation (subcutaneous injection of 5 mg kg^{-1} ketoprofen) and provided local (0.5% Marcaine solution injected under the scalp) and general analgesia (intraperitoneal injection of 0.1 mg kg^{-1} buprenorphine). A circular piece of scalp was removed and the underlying bone was cleaned and dried. The periostium was removed with a dental drill and the exposed skull was covered with a thin layer of cyano-acrylic primer (Crazy glue). A custom-machined titanium frame was cemented to the skull with dental acrylic (Lang Dental).

Afferents from the somatosensory cortex were labelled with virus expressing tdTomato[33] (rAAV2/1-CAG-tdTomato; 20 nl at 300- and 550-μm depths). The C2 barrel was targeted based on intrinsic signal imaging[28]. The virus was injected with a custom, piston-based, volumetric injection system (based on a Narishige, MO-10 manipulator)[46]. Glass pipettes (Drummond) were pulled and bevelled to a sharp tip (outer diameter of 30 μm). Pipettes were back-filled with mineral oil and front-loaded with viral suspension immediately before injection.

A craniotomy was made over the vM1 of the left hemisphere (size, 3 × 2 mm; centre relative to Bregma: lateral, 0.8 mm; anterior, 1 mm) (Fig. 2a–d). These coordinates were previously determined using intracortical microstimulation[8,16,18], by mapping axonal projections from vS1 in vM1 (refs 8, 47), and by trans-cellular labelling with pseudorabies virus (data not shown). Neurons underlying the craniotomy were labelled by injecting rAAV2/1-Syn-GCaMP3 (produced by the University of Pennsylvania Gene Therapy Program Vector Core). The brain was covered with agar (2%). Between four and eight sites (10–15 nl per site; depth, 150–210 μm; rate, 10 nl per minute) were injected per craniotomy.

The imaging window was constructed from two layers of standard microscope coverglass (Fisher; number 2 thickness, 170–210 μm), joined with an ultraviolet curable optical glue (NOR-61, Norland). A larger piece was attached to the bone and a smaller insert was fitted snugly into the craniotomy (Fig. 2b, d). The bone surrounding the craniotomy was thinned to allow for a flush fit between the insert and the underlying dura.

After virus injection, the glass window was lowered into the craniotomy. The space between the glass and the bone was sealed off with a thin layer of agar (2%), and the window was cemented in place using dental acrylic (Lang Dental). At the end of the surgery, all whiskers on the right side of the snout except row C were trimmed. The mice recovered for 3 days before starting water restriction. Imaging sessions started 14–21 days after the surgery.

Behaviour. We designed an object-detection task, with three goals in mind: first, animals should be able to learn the task quickly, in a few days; second, the sensory (whisker contacts and forces) and motor (whisking, licking) behaviours needed to be tracked at high spatial and temporal resolutions throughout learning; third, we wanted to detect neurons in the motor cortex whose activity patterns might be shaped by sensory input. Because different object locations produce different somatosensory stimuli, we presented the object in several locations. Neural activity levels that depend on object location then indicate the coding of sensory variables.

Behavioural training began after the mice had restricted access to water for at least 7 days (1 ml per day)[5,28]. The behavioural apparatus was designed to fit under a custom-built two-photon microscope (https://openwiki.janelia.org/wiki/display/shareddesigns/). All behavioural training was performed under the microscope while imaging neural activity. In a pre-training session mice learned to lick for water rewards from a lick port (~100 rewards). At the same time the brain was inspected for suitable imaging areas. Fields of view were restricted to zones where expression of GCaMP3 and tdTomato (axons from vS1) overlapped (Fig. 2a–d). To escape the vasculature near the midline, imaging was typically performed towards the lateral edge of vM1. Mice with excessive brain movement, limited virus infection or impaired optical access (bone growth or large blood vessels in the vS1 axon projection zone) were excluded from the study.

During the first behavioural session (session 1) the pole was positioned within the range of the whiskers' resting position, thereby increasing the chance of a whisker–pole collision. As soon as performance reached $d' > 1$ the pole was advanced to a more anterior position (~0.5 mm from whisker resting position), forcing the mouse to sample actively for the pole. The target position was adjusted for every session. In expert mice, multiple target positions, all within reach of the whiskers, were introduced to study the effects of object location (Supplementary Figs 8–11, 13 and 15, and Supplementary Table 1).

Reversible inactivation. To inactivate vM1 the GABA (γ-aminobutyric acid) agonist muscimol was injected into the imaging area in expert mice. A small hole was drilled through the imaging window to allow access for a glass injection pipette. Muscimol hydrobromide (Sigma-Aldrich) was dissolved in saline (5 μg μl^{-1}) and 50 nl were injected slowly (10 nl per min) at depths of 500 and 900 μm under the pia[27]. The animals were left to recover for 2 hours before the behavioural session. Inactivation caused a complete absence of fluorescence transients in the imaged field of view (data not shown). Similar methods were used to inactivate vS1 (Supplementary Fig. 1)[27].

Imaging. GCaMP3 was excited using a Ti-Sapphire laser (Chameleon, Coherent) tuned to $\lambda = 1{,}000$ nm. We used GaAsP photomultiplier tubes (10770PB-40, Hamamatsu) and a 16× 0.8 NA microscope objective (Nikon). The field of view was 450 × 450 μm (512 × 256 pixels; pixel size, 0.88 × 1.76 μm), imaged at 4 Hz. The microscope was controlled with *ScanImage*[48] (http://www.scanimage.org). The average power for imaging was <70 mW, measured at the entrance pupil of the objective. For each mouse the optical axis was adjusted to be perpendicular to the imaging window. Imaging was continuous over behavioural sessions lasting approximately 1 h (average, 53 min; range, 24–72 min). Bleaching of GCaMP3 was negligible. Slow drifts of the field of view were corrected manually approximately every 50 trials using a reference image.

Image analysis. To correct for brain motion we used a line-by-line correction algorithm (similar to a method used previously[49], but based on a correlation-based error metric). First, we averaged five consecutive images showing the smallest luminance changes (chosen from the approximately 40 images comprising a behavioural trial). Each line of each frame was then fit to this reference image using a piecewise rigid gradient-descent method.

To align all trials within one session, the average of the trial showing the smallest luminance changes was used as the session reference and all other trials were aligned using normalized cross-correlation-based translation.

To extract fluorescence signals from individual cells, regions of interest (ROIs) were drawn based on neuronal shape (individual neurons appeared as fluorescent rings; Supplementary Fig. 5). Mean, maximum intensity and standard deviation values of all frames of a session were used to determine the boundaries of the neurons. An automated method was used to align the ROIs across sessions. For each ROI, a small square (50 × 50 pixels) around the ROI was selected. Displacements across sessions were calculated by computing the point at which the normalized cross-correlation for this square and the average image of the day peaked. For each ROI, its displacement vector was compared to that of its five nearest neighbours. In cases in which the displacement exceeded seven times the median of the neighbours' displacements, it was set to the median and flagged for manual inspection. The displacements of all ROIs defined a warp field for the entire image.

The pixels in each ROI were averaged to estimate the fluorescence of a single cell. The cell's baseline fluorescence, F_o, was determined in an iterative manner. First, we estimated the probability distribution function (PDF) of raw fluorescence for each ROI and centred it at its peak (that is, the peak was assigned a value of 0). A 'cutoff value' was calculated by choosing the points below the PDF's peak and determining the value above which 90% of these values lay (which was negative owing to our centring procedure). Cells were 'moderately active' if at least 1% of their fluorescence was above twice the absolute value of this cutoff value (that is, the PDF had a long positive tail). Cells were 'highly active' if the density at this cutoff value relative peak density exceeded 0.1 (that is, the PDF's positive tail was not only long but also fat). All other cells were 'sparsely active'. The initial F_o estimate was generated by taking a 60-s sliding window over raw fluorescence and using the 50th, 20th or 5th percentile as F_o for sparsely, moderately and highly active cells, respectively. Using this first F_o estimate, we computed a preliminary $\Delta F/F$ (defined as $(F - F_o)/F_o$) and extracted events based on a threshold (three times the median absolute deviation (MAD)). An event period was defined as starting 2 s before the peak during a cross of threshold and ending 5 s after the peak. In the subsequent F_o estimation procedure, F_o was only estimated for periods without events, and determined using linear interpolation for periods during events. The final $\Delta F/F$ trace used for all subsequent analysis was computed using this F_o trace. To produce an event vector from the $\Delta F/F$ trace and thereby minimize the temporal distortions caused by GCaMP3 dynamics[34], we used a non-negative deconvolution method (Supplementary Fig. 5)[36].

Calcium imaging with genetically encoded indicators was crucial for tracking the same neurons across multiple sessions. Furthermore, using imaging it is possible to sample neural activity densely within a region. However, current calcium indicators, including GCamP3, are not sufficiently sensitive to detect single action potentials *in vivo* and, as a consequence, activity in neurons with very low firing rates was probably missed[28,34]. Our analysis therefore focuses on relatively active neurons. In addition, the slow dynamics (on the order of 100 ms) of the calcium indicator limits the conclusions that can be drawn about connectivity and causality from imaging data.

Approximately 80% of cortical neurons are pyramidal[50]. GABAergic interneurons produce much smaller activity-dependent fluorescence changes than

pyramidal neurons, presumably because of their short action potentials and high concentrations of endogenous calcium buffer[51], and their activity was not likely to be detected using GCaMP3[28]. For these reasons, the vast majority of active neurons detected with our methods were probably excitatory pyramidal neurons.

Long-term expression of GCaMP3. AAV-mediated expression of GCaMP3 provides the high expression levels that are necessary for *in vivo* cellular imaging. However, expression continues to increase over months, which can lead to compromised cell health[34,52], and this correlates with breakdown of nuclear exclusion. Over the time course of our experiments (up to 4 weeks of expression), no more than 2% of the cells in the imaged field of view showed nuclear GCaMP3. These neurons were excluded from analysis. In addition, overall event rates were stable across time (Supplementary Fig. 17).

Several observations indicate that imaging did not damage the brain. First, because of the brightness and photostability of GCaMP3 we were able to use low average power. Second, there was no evidence for tissue damage (Supplementary Fig. 3). Third, task-related activity increased with learning in a specific manner, so that some representations (for example, licking) increased, whereas other representations did not change (whisking) (Fig. 6). These learning-related changes are inconsistent with nonspecific rundown.

Changes in intracellular calcium are necessary to trigger a variety of forms of cellular plasticity. Could GCaMP3 expression interfere with synaptic plasticity? The strength of calcium buffering (buffer capacity) can be estimated as buffer concentration divided by its dissociation constant (K_d)[53]. High concentrations (>200 μM) of strong (K_d, 170 nM) calcium buffer (for example, BAPTA) are required to block synaptic plasticity[54,55]. We estimated the concentration of GCaMP3 (K_d, 660 nM)[34] under our experimental conditions. We collected acute brain slices from mice that had been used in long-term imaging experiments. We then compared cellular fluorescence at saturating calcium levels, induced by high external K^+ (20–30 mM) to calibrated GCaMP3 solutions (in standard K^+-based internal solution normally used for whole-cell recording). Four weeks of expression in L2/3 pyramidal neurons of the visual cortex yielded 76 μM of GCaMP3 (ref. 52). Seven weeks of expression in vM1 gave 130 μM of GCaMP. These results suggest that GCaMP3 produces lower buffer capacity than BAPTA concentrations that are known not to perturb synaptic plasticity (buffer capacities, <200 versus >1200). Consistent with this, expression of GCaMP3 did not perturb induction of long-term potentiation in hippocampal brain slices (Supplementary Fig. 4) (GCaMP3 concentration was 15 μM, determined as above).

We further tested whether GCaMP3 expression level influenced the plasticity of neuronal responses. The relative baseline fluorescence measured in individual neurons was constant across days and it was therefore a good indicator of GCaMP3 expression. We calculated the probability that a classified cell remained active and retained its classification (that is, was stable). We compared stability in the 25% brightest and dimmest neurons. Dim and bright cells were similarly stable (dim cells, 65% stable; bright cells, 60% stable; $\chi^2 = 0.39$; $P > 0.5$). This analysis suggests that under our conditions GCaMP3 does not obviously perturb cellular plasticity *in vivo*.

Other measurements also suggest that plasticity was not obviously impaired by long-term expression of GCaMP3. Circuit function is shaped by ongoing plasticity, integrated over the recent past. Neurons with long-term expression of GCaMP3 generally show normal circuit properties. Orientation and direction selectivity are normal in GCaMP3-expressing L2/3 neurons in mouse V1 (ref. 52) and hippocampal place cells are normal in CA1 neurons in the hippocampus[56]. The sparseness and response types of L2/3 neurons in vS1 are indistinguishable when measured with electrophysiological methods or GCaMP3 (ref. 28). Finally, in our experiments L2/3 neurons showed specific learning-related changes in activity *in vivo* (Figs 4–6).

Whisker tracking. Whiskers were illuminated with a high-power light-emitting diode (LED) (940 nm, Roithner) and condenser optics (Thorlabs). Images were acquired through a telecentric lens (0.36×, Edmund Optics) by a high-speed CMOS camera (EoSense CL, Mikrotron, Germany) running at 500 frames per s (640 × 352 pixels; resolution, 42 pixels per mm). Image acquisition was controlled by Streampix 3 (Norpix). The whisker position and shape were tracked using automated procedures[27]. Whiskers are cantilevered beams, with one end embedded in the follicle in the whisker pad. The mechanical forces acting on the follicles can be extracted from the shape changes after contact between whisker and object. For example, a change in curvature at point p along the whisker is proportional to the force applied by the pole on the whisker[30]: $F \sim \Delta\kappa_p\, y_p$, where y_p is the bending stiffness at p (approximately 3 mm from the follicle). We thus present forces on the whiskers as the change in curvature, $\Delta\kappa$. These forces underlie object localization[27,31]. $\Delta\kappa$ was determined using a parametric curve comprising second-order polynomial fits to the whisker backbone. Periods of contact between whisker and object (touch) were detected based on the nearest distance between whisker and object, and $\Delta\kappa$. A total of ~13,000,000 whisker video images, comprising ~7,500 behavioural trials, were analysed for this project.

Expert mice contacted the pole multiple times with one or several whiskers (average number of contacts for the dominant whisker, 8; range 0–19) before their decision (signalled by an answer lick on correct go trials).

Behavioural features. We analysed neural activity with respect to several behavioural features. Licks were detected with a lickometer[27] and lick rate (Hz) was defined as the inverse of the inter-lick interval. Our imaging rate (4 Hz) was slower than the rapid components of rhythmic whisking (10–20 Hz). In addition, motor cortex neurons primarily code for the slowly varying whisking variables, set-point and amplitude[29,39]. Whisker set-point was the low-pass filtered (6-Hz) whisker angle. Whisker amplitude was defined as the Hilbert transform[29] of the absolute value of the band-pass filtered (6–60-Hz) whisker angle (Fig. 1d). Because whiskers move mostly together[27], set point and amplitude were averaged across all whiskers. The time derivatives of whisker set-point and amplitude were used as independent features. $\Delta\kappa$ was measured during the sampling period. Protraction touch (positive curvature changes), retraction touch (negative curvature changes) and absolute values were treated separately. All behavioural features were down-sampled to match the image acquisition rate (4 Hz). Mean and maximum values were calculated for each feature in a 250-ms window centred on the middle of the new sampling point.

Decoding behavioural variables. The relationship between the calcium activity x_i of the ith neuron and the jth behavioural variable y_j can be characterized as an encoding description $P(x_i|\, y_j)$ or a decoding description $P(y_j|x_i)$. The encoding description specifies how much of neuronal activity can be accounted for by behavioural variables. The decoding description specifies how behavioural variables can be derived from the activity of one neuron or neuronal populations. Here, we focused on the decoding description.

We used machine learning algorithms to decode behavioural features based on activity. The input to the algorithm was the event rate (that is, deconvoluted $\Delta F/F$). To predict sensory input we also used time-shifted future activity. For motor variables we used both past and future activity, as neural activity could reflect motor commands, corollary discharges or reafferent input.

The goal of the decoder algorithm was to find a mapping $\hat{y}_j(t_k) = f\left[x_i(t_{k-l}), \ldots, x_i(t_k), \ldots, x_i(t_{k+p})\right]$ that best approximates $y_j(t_k)$ for all t_k (discretized time in units of 0.25 s, corresponding to the imaging rate); l and p represent the maximum negative and positive shifts of the activity respectively.

We concatenated trials to generate a vector $\bar{t}$ of time-binned data. We used $l = 2$ and $p = 0$ for sensory variables, and $l = 2$ and $p = 2$ for sensory-motor variables (corresponding to time-shifts up to 0.5 s). The dimensionality of the input variables is $l + p + 1$. To simplify the notation, we define the vector $\bar{x}_{i,n}$ as the activity of cell i at all times shifted n frames to the future. The algorithm was trained on a subset of trials (the training set; 80%) and evaluated on a separate set of test trials (20%). We repeated this procedure five times to obtain a prediction for all trials[38].

The accuracy of decoding was evaluated using the Pearson correlation coefficient (ρ) between the model estimate and the data. The explained variance is $R^2 = \rho^2$ (range 0–1). R^2 was calculated separately for each trial type (that is, hit, correct rejection, miss and false alarm). Treating trial types separately was critical to disambiguate the relationship between different behavioural variables and activity. For example, we observed large-amplitude whisking during licking, which complicates the classification of neuronal responses. However, during correct rejection trials, licking was absent and whisking present, allowing classification. Similarly, in trained animals, touch and licking occurred with short latencies in hit trials (Figs 1 and 5). In contrast, touch was absent in false alarm trials.

Decoding was carried out using the random forests algorithm[38,57], a multivariate, non-parametric machine learning algorithm based on bootstrap aggregation (that is, bagging) of regression trees. We used the TreeBagger class implemented in Matlab. TreeBagger requires only a few parameters: the number of trees ($N_{trees} = 128$), the minimum leaf size (minleaf = 5), the number of features chosen randomly at each split ($N_{split} = N_{features}/3$; the typical value used by default). These parameters were chosen as a trade-off between decoder accuracy and computation time. We did not observe much improvement in decoding accuracy for $N_{trees} > 32$ and minleaf <10 (data not shown).

Classification of response types. We measured the R^2 between each measured behavioural variable (for example, whisking speed, lick rate and whisking set-point) and each cell's decoder prediction for all the trials and for each trial type. We considered only cells with more than one event in a session. In addition, for sessions with multiple-pole positions we used an analysis of variance (ANOVA) to determine whether the contact-evoked calcium response was different for the different pole position (Supplementary Figs 8–11, 13 and 15). We grouped the behavioural variables in larger categories such as whisking (for example, whisking

amplitude, set-point and speed), lick rate and touch (for example, touch per whisker, rate of change of forces and absolute magnitude). We considered the best R^2 set for each of the three behavioural categories. Alternatively, all cells were manually classified based on trial-to-trial calcium transients and behavioural prediction for each trial type. For most cells (>82%) classification was unambiguous based on the decoder R^2 values. The remaining cells were more accurately classified based on a rarer trial type (typically false alarm trials). Three of the authors independently arrived at consistent classifications.

Population decoding. For decoding neural populations (Figs 3 and 6) we considered all neurons showing at least one event and created an input vector of size $N_{\text{neurons}} \times (l + p + 1)$. We trained the random forest algorithm to decode each of the behavioural variables and evaluated the quality of the fit as before.

With the model based on data from one day we tested decoding of behavioural variables on another day. To compare data between two different days, we normalized the neural activity and the behavioural variables using a *z*-score transformation (by subtracting the mean and dividing by the standard deviation). In addition, some cells were active on one day but not on other days. We labelled these neurons as missing data.

Measurement of synaptic plasticity in brain slices. Rat hippocampal slice cultures were prepared at postnatal days 4 and 5 (ref. 58). Plasmids encoding GCaMP3 and cerulean under the control of a human synapsin 1 promoter were electroporated into single CA1 pyramidal neurons after 18 days *in vitro* (1:1 ratio; 50 ng μl^{-1} each) (modified from ref. 59). Recordings were taken 3–7 days after transfection. GCaMP3 was mainly excluded from the nucleus and cell morphology was indistinguishable from neurons expressing cerulean alone. Paired whole-cell recordings from CA1 and CA3 pyramidal cells were made at room temperature (21–23 °C), using 3–4 MOhm pipettes containing (in mM): 135 K-gluconate, 4 $MgCl_2$, 4 Na_2-ATP, 0.4 Na-GTP, 10 Na_2-phosphocreatine, 3 ascorbate and 10 HEPES (pH 7.2). ACSF consisted of (in mM): 135 NaCl, 2.5 KCl, 4 $CaCl_2$, 4 $MgCl_2$, 10 Na-HEPES, 12.5 D-glucose and 1.25 NaH_2PO_4 (pH 7.4). Excitatory postsynaptic currents were measured at −65-mV holding potential.

46. Petreanu, L., Mao, T., Sternson, S. M. & Svoboda, K. The subcellular organization of neocortical excitatory connections. *Nature* **457,** 1142–1145 (2009).
47. Porter, L. L. & White, E. L. Afferent and efferent pathways of the vibrissal region of primary motor cortex in the mouse. *J. Comp. Neurol.* **214,** 279–289 (1983).
48. Pologruto, T. A., Sabatini, B. L. & Svoboda, K. ScanImage: flexible software for operating laser-scanning microscopes. *Biomed. Eng. Online* **2,** 13 (2003).
49. Greenberg, D. S. & Kerr, J. N. Automated correction of fast motion artifacts for two-photon imaging of awake animals. *J. Neurosci. Methods* **176,** 1–15 (2008).
50. Gonchar, Y., Wang, Q. & Burkhalter, A. Multiple distinct subtypes of GABAergic neurons in mouse visual cortex identified by triple immunostaining. *Front. Neuroanat.* **1,** 3 (2007).
51. Kerlin, A. M., Andermann, M. L., Berezovskii, V. K. & Reid, R. C. Broadly tuned response properties of diverse inhibitory neuron subtypes in mouse visual cortex. *Neuron* **67,** 858–871 (2010).
52. Zariwala, H. A. *et al.* A cre-dependent GCaMP3 reporter mouse for neuronal imaging *in vivo*. *J. Neurosci.* **32,** 3131–3141 (2012).
53. Maravall, M., Mainen, Z. M., Sabatini, B. L. & Svoboda, K. Estimating intracellular calcium concentrations and buffering without wavelength ratioing. *Biophys. J.* **78,** 2655–2667 (2000).
54. Nevian, T. & Sakmann, B. Spine Ca^{2+} signaling in spike-timing-dependent plasticity. *J. Neurosci.* **26,** 11001–11013 (2006).
55. Gordon, U., Polsky, A. & Schiller, J. Plasticity compartments in basal dendrites of neocortical pyramidal neurons. *J. Neurosci.* **26,** 12717–12726 (2006).
56. Dombeck, D. A., Harvey, C. D., Tian, L., Looger, L. L. & Tank, D. W. Functional imaging of hippocampal place cells at cellular resolution during virtual navigation. *Nature Neurosci.* **13,** 1433–1440 (2010).
57. Breiman, L. Random forests. *Mach. Learn.* **45,** 5–32 (2001).
58. Stoppini, L., Buchs, P. A. & Muller, D. A. A simple method for organotypic cultures of nervous tissue. *J. Neurosci. Methods* **37,** 173–182 (1991).
59. Rathenberg, J., Nevian, T. & Witzemann, V. High-efficiency transfection of individual neurons using modified electrophysiology techniques. *J. Neurosci. Methods* **126,** 91–98 (2003).